Modeling and Synthesizing Infrared Ocean Clutter

Kim T. Constantikes

The next generation of ship defense missiles will need to engage stealthy, passive, sea-skimming missiles. Detection and guidance will take place against a background of sea surface and horizon, which can present significant clutter problems for infrared seekers, particularly when targets are comparatively dim. We need a variety of sea clutter models: statistical image models for signal processing algorithm design, clutter occurrence models for systems effectiveness assessment, and constructive image models for synthesizing very large field-of-view images with high spatial and temporal resolution. Existing models of sea surface and atmospheric optical properties, sea surface roughness, and image formation can predict the average brightness of the sea surface from a seeker's perspective. Estimates of the likelihood of sea glint in the seeker field of view use nonparametric weather models. We discuss two feasible approaches to image synthesis: Markov random field models, which can capture higher-order statistical moments of clutter but are problematic, and first-principle models of water waves and light transport, which provide a computationally intensive clutter model. We have consolidated existing models of average brightness and have developed new models of spatial and temporal variation.

INTRODUCTION

Models are used extensively in the design and evaluation of infrared seeker and tracking systems. Background and target source models and atmospheric propagation models can provide approximations of the radiance at the aperture of a seeker. A model of the image formation process approximates seeker optics, detector diode, and scan motion to construct detector output signals given the radiance at the optics aperture. A simulation of the signal processor takes detector signals and generates target detections and locations. Of all these models, the background model, often char-

acterized as a correlated Gaussian noise model, is the least well known.

The models that we desire are somewhat different. We need a model of the detector outputs given a small number of environmental parameters and target parameters. Such a model, along with target dynamics and probability laws for the environmental parameters, could be used to optimize signal processor design empirically. We also need a model that provides the probabilities of detection, false alarm, and pointing errors as a function of the environmental parameters.

This model could be used in conjunction with guidance simulations to calculate Monte Carlo estimates of hit probabilities. In addition, we need a constructive model of the radiance at the seeker aperture, i.e., given a particular environment, we need to synthesize a realization of the scene random process. This model could be used for seeker optimizations such as spectral band selections, and for generating test images for laboratory evaluation of the seeker.

Why is modeling needed? Because actual measurements are at the mercy of nature, expensive, and sometimes technically infeasible. For example, a validated propagation model combined with a validated target signature model can produce signatures over a wider range of conditions than one could reasonably hope to measure in the field, and at a lower cost. A particular technological problem is background measurements for use in laboratory testing. Ideally, such measurements would have about 5 times the spatial and temporal resolution of the seeker under test, and the total field of view would be equal to the seeker search field of view. These requirements are not met by available imaging devices, and so we are forced to alternatives such as patching scenes together from small images or synthesizing scenes for nearly literal representations.

What should be modeled? Consider the model for radiance at the seeker aperture. The waveband of interest is 3 to 5 μm,* which is much smaller than the millimeter-sized features of the sea roughness. Thus the radiance model need not take into account physical optics of reflection from the sea surface. Even if it did, the signal model of detector output voltage as a function of environment would be unchanged. Given equivalent models, we select the simplest model that preserves the essential phenomena, avoiding inadequate or inefficient models. For example, it is almost always assumed that clutter (as measured at detector outputs) is a jointly Gaussian process, and hence the mean and covariance matrix of the clutter is sufficient for predicting the false alarm rate (FAR) for a linear detection scheme. Such an assumption can result in grossly overoptimistic predictions of FAR. In principle, and apparently in practice for the sea surface imaged in good visibility, the joint distribution function of the clutter process is essential. On the other hand, clutter models for low-altitude viewing of the horizon can be very simple; the optical thickness of the atmosphere is

great, and seeker clutter may be dominated by photon fluctuations, which are easily modeled as independent Gaussian noise.

We are most concerned with the reflection of solar (or lunar) irradiance to the seeker because in the midwave infrared the solar irradiance of the surface, and hence the radiance reflected to the seeker, can be much greater than the emission of graybodies at ambient temperature. What are the statistical characteristics of the "glint corridor"? How often may we encounter it in tactical situations? The phenomenology of glint clutter can be quite variable (see the boxed insert on glint phenomena).

Although many constituents of the models we desire are available, they are not complete. Even the jointly Gaussian clutter model of sea background is incomplete because the prediction of the covariance matrix from first principles is problematic. This article considers the construction and results of models of mean and variance of radiance for midwave infrared images taken from low altitude (about 100 m) and looking toward the horizon. We first discuss our empirical modeling approach and then describe a computational physical model and preliminary model outputs. Many of the results can be readily extended to other sea background scenarios.

BASIC MODELS

Several factors contribute to apparent radiance at the sensor (see the boxed insert on infrared seeker performance models).[†] Direct solar radiation is attenuated by the Earth's atmosphere (E_{Sun}), reflected by the sea surface, and then attenuated again as it propagates to the sensor (L_{Sun}). Skylight is reflected to the sensor (L_{sky}). Radiation scattered by the atmosphere can enter the sensor aperture (L_{scat}). The emissions of the sea surface (L_{sea}) and sensor-to-surface path (L_{path}), as well as the associated attenuations, contribute as well. The spectral radiance $L(\lambda)$ at the sensor is then given by

$$L(\lambda) = L_{path}(\lambda) + L_{sky}(\lambda) + L_{Sun}(\lambda) \\ + L_{sea}(\lambda) + L_{scat}(\lambda). \tag{1}$$

For specific wavebands, we wish to compute the apparent-effective radiance by including both the spectral

---

* The 3- to 5-μm range is known as the midwave infrared. This band is useful in detecting small temperature differences of objects. In particular, for $L_m(T)$ and $L_l(T)$, the mid- and long-wave radiances of a blackbody at temperature T, the contrast radiance for 300 to 310 K is twice as large in the midwave as in the long wave:

$$\frac{L_m(310) - L_m(300)}{L_m(300)} = 0.42; \quad \frac{L_l(310) - L_l(300)}{L_l(300)} = 0.17.$$

[†] In this discussion, apparent quantities take into account path attenuation effects, and effective quantities take into account sensor spectral sensitivity. Standard radiometric units are used, i.e., irradiance is incident radiant flux in W/cm^2, and radiance is brightness in W/cm^2·sr.


GLINT PHENOMENA

This collection of infrared images of glint clutter comes from different imagers and shows various geometries. Image (a) was taken from about 100 ft above sea level at Huntington Beach, California, using a Cincinnati Electronics IRC-160 focal plane array camera. The spectral band is a small fraction of the midwave, the field of view is about $4 \times 3°$, and the detector instantaneous field of view is about 0.5 mrad. Clutter power in this image is about 10 times the noise effective radiance of a 2-in. aperture seeker. Image (b) is a portion of an image taken at Pt. Loma, California, about 300 ft above sea level. The image was taken using the Massachusetts Institute of Technology's Infrared Measurements System. This sensor has very high spatial resolution and a slow scanning rate. The image fragment here is about $8 \times 4°$. Note how the clutter variance decreases sharply as range increases, and that a homogeneous bright area extends down about 0.5° from the horizon.

Images (c) through (e) were taken from an airborne platform using the Hughes Missile Systems Company Infrared Data Acquisition System midwave imager, looking at an aircraft flying close to sea level. In (c) the background does not include glint. In (d) the aircraft is at the edge of the glint corridor, and in (e) the aircraft is in the middle of the glint corridor. Note that gravity wave structure is apparent in images (c) through (e). The target aircraft can be located by eye in (c) and (e) but not in (d). Since the clutter in this geometry is primarily gravity wave self-shadowing, the correlation times of clutter are long, and a moving target indication scheme applied to a time series of images (d) will detect target aircraft motion with respect to the clutter. Image (f) was taken at Pt. Loma from near sea level with a Mitsubishi platinum silicide camera. Note the small, isolated bright spots in the midground of the image. The time series of these images shows correlation times for these glints to be about 70 ms. In this case, moving target indication would work poorly, if at all.

The images are courtesy of the following: (a) Hughes Missile Systems Company, (b) Lincoln Laboratory, (c)–(e) Hughes Missile Systems Company, and (f) Raytheon Corp.

(a)

(b)

(c)

(d)

(e)

(f)
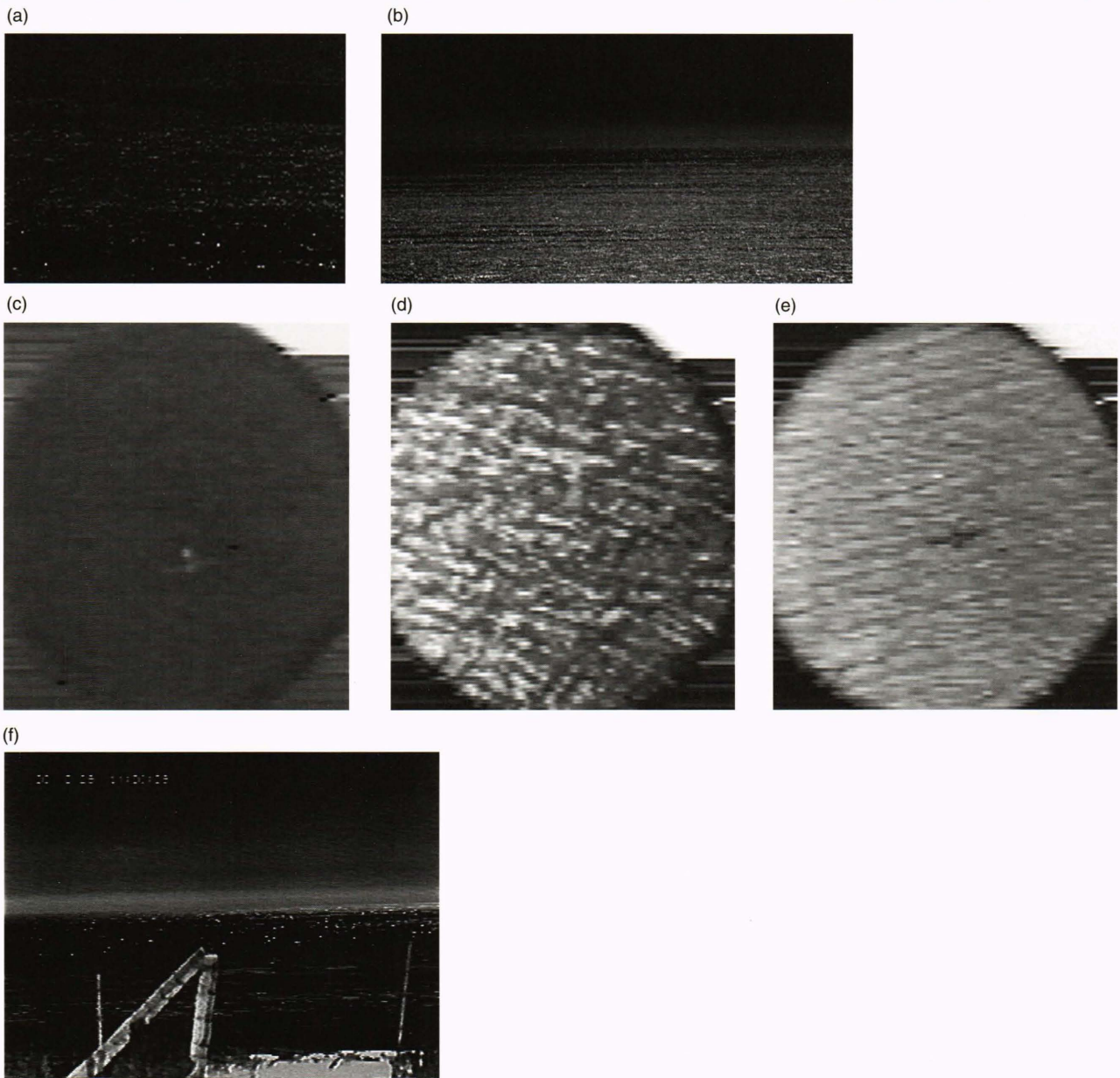
COMPONENT MODELS OF AN INFRARED SEEKER PERFORMANCE MODEL

To predict the detection and false alarm performance of an infrared seeker, we must model the target signature, emission and propagation in the atmosphere, illumination and emission of surfaces, scattering and reflection, and image formation. In addition, we must emulate signal processing of detector outputs. Target signature models are provided as part of system specifications. Atmospheric models include MODTRAN[1] and LOWTRAN.[2] The ocean surface scattering model for mean radiance is the Cox and Munk model[3] with the Saunders self-shadowing correction.[4] These models are combined to predict the radiance at the seeker aperture, $L(\phi, \theta)$, as a function of viewing geometry, target, atmospheric parameters, and meteorological parameters. The image formed by the seeker is a set of detector outputs sampled in time [$V(n\Delta t)$]. These signals are processed by an emulation of seeker signal processing to generate detections and tracks. These, in turn, are modeled statistically to system level performance measures of detection probability, false alarm probability, and pointing error probability (P_d, P_{fa}, P_ϵ). Once the complete model is formulated, we can study missile system performance by Monte Carlo evaluation of probability integrals involving the environmental parameters and engagement geometry.
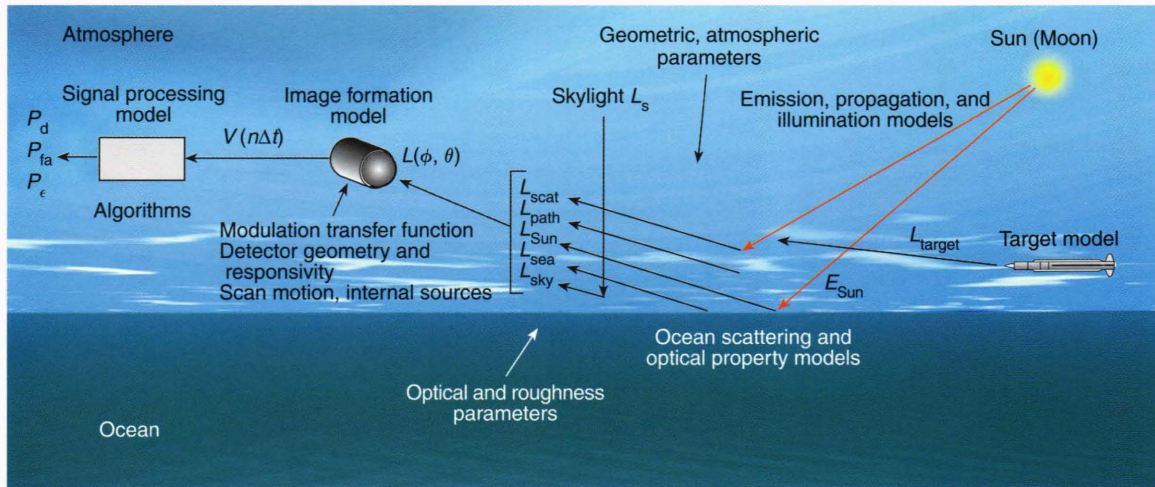
path attenuation and the spectral characteristics of the sources and detectors. In practice, all of the radiance quantities in Eq. 1 are complicated functions of atmospheric conditions, so the path attenuation, path radiance, direct solar irradiance, scattered solar radiance, and sky radiance are computed using standard atmospheric models within LOWTRAN7.[2] The directly reflected solar component is, for an assumed rectangular band, given by

$$L_{Sun} = \int_{\lambda_l}^{\lambda_u} \xi(\lambda)\, E_{Sun}(\lambda)\, \tau_{path}(\lambda)\, d\lambda , \qquad (2)$$

where $E_{Sun}(\lambda)$ denotes the spectral irradiance of the sea surface by the Sun, $\tau_{path}(\lambda)$ is the spectral transmittance of the surface-to-sensor path, and λ_u and λ_l are the upper and lower spectral band limits, respectively. $\xi(\lambda)$ is the sea surface scattering parameter, a function of viewing geometry, reflectance, and wind speed. We approximate this integral, and all other spectral integrations herein, by assuming spectral dependencies to be slowly varying, i.e., nearly constant:

$$
\begin{aligned}
L_{Sun} &\approx \frac{1}{\lambda_u - \lambda_l} \int_{\lambda_l}^{\lambda_u} \xi(\lambda)\, d\lambda \int_{\lambda_l}^{\lambda_u} E_{Sun}(\lambda)\, d\lambda \\
&\times \frac{1}{\lambda_u - \lambda_l} \int_{\lambda_l}^{\lambda_u} \bar{\tau}_{path}(\lambda)\, d\lambda = \bar{\xi}\, E_{Sun}\, \bar{\tau}_{path} ,
\end{aligned}
\qquad (3)
$$

where overbars denote the mean value of the quantity over the spectral band of interest, and the absence of the spectral parameter in radiance or irradiance signifies that the spectral dependence has been integrated over a band of interest.

The reflected skylight contribution is computed from the sky dome radiance, L_s, using a geometric factor G, which includes reflectance, as follows:

$$L_{sky} \approx \overline{G} L_s \bar{\tau}_{path} . \qquad (4)$$

We introduce a sea surface emissivity ϵ to account for the spatially averaged reflectance (averaged over the random surface orientations) for a given viewing direction. Then we have

$$L_{sea} \approx \bar{\epsilon} L_{bb} \bar{\tau}_{path} , \qquad (5)$$

where L_{bb} is the radiance of a blackbody at the sea temperature. In the spectral bands of interest and the given geometry, scattered solar radiation is much less than path radiance,[5] so we set L_{scat} equal to zero. Now assuming that the skylight is atmospheric emission with the same radiance as the sea surface blackbody, i.e., $L_{bb} = L_s$, and assuming an optically thick ocean, we can use Kirchhoff's law[6] (thermodynamic equilibrium) to combine the geometric factor and emissivity. Kirchhoff's law states that detailed thermodynamic balance requires that the sum of spectral emissivity, transmittivity, and reflectivity be one. Our assumption that the ocean is optically thick is equivalent to assuming that the transmittivity is zero. Thus

$$L_{sky} + L_{sea} \approx (\bar{\epsilon} + \overline{G}) L_{bb} \bar{\tau}_{path} \approx L_{bb} \bar{\tau}_{path} . \qquad (6)$$

The validity of these assumptions is borne out by LOWTRAN7 computations, in particular when the sea temperature equals the boundary layer temperature and the dis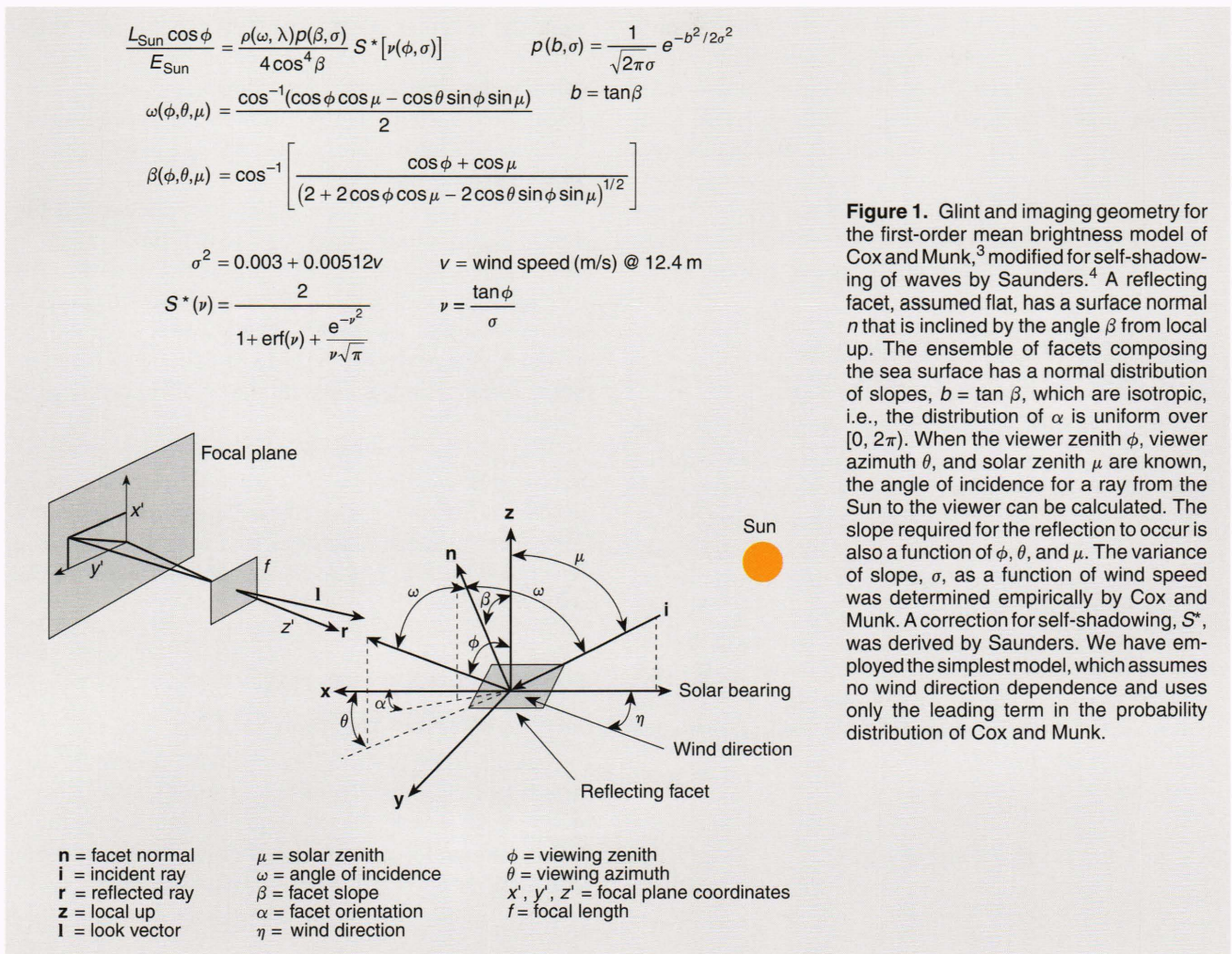tribution of wave slopes is small, so that the geometric factor heavily weights the sky radiation emanating from around the specular direction. Finally, we have

$$L \approx L_{path} + \left(\bar{\xi} E_{Sun} + L_{bb} \right) \bar{\tau}_{path} \approx L_{bb\text{-}ae} + \bar{\xi} E_{Sun} \bar{\tau}_{path}, \qquad (7)$$

where the quantities on the right-hand side are functions of wind speed and viewing geometry, and $L_{bb\text{-}ae}$ is the apparent-effective blackbody radiance of the sea surface seen through the marine boundary layer.

The scattering of solar irradiance from the sea surface has been modeled by Cox and Munk[3] and modified to account for self-shadowing of waves by Saunders.[4] The first-order model assumes a Gaussian distribution of wave slopes, where slope variance is determined by wind speed. Figure 1 shows the geometry of reflecting facets and the associated formulas. The scattering parameter in Eq. 3 is then given by

$$\frac{L_{Sun}(\lambda)}{E_{Sun}(\lambda)} \equiv \xi(\lambda) = \frac{\rho(\omega,\lambda)p(\beta,\sigma)}{4\cos^4(\beta)\cos(\phi)} S*\left[\nu(\phi,\sigma)\right], \qquad (8)$$

$$\frac{L_{Sun}\cos\phi}{E_{Sun}} = \frac{\rho(\omega,\lambda)p(\beta,\sigma)}{4\cos^4\beta} S*\left[\nu(\phi,\sigma)\right] \qquad p(b,\sigma) = \frac{1}{\sqrt{2\pi}\sigma} e^{-b^2/2\sigma^2}$$

$$\omega(\phi,\theta,\mu) = \frac{\cos^{-1}(\cos\phi\cos\mu - \cos\theta\sin\phi\sin\mu)}{2} \qquad b = \tan\beta$$

$$\beta(\phi,\theta,\mu) = \cos^{-1}\left[\frac{\cos\phi + \cos\mu}{(2 + 2\cos\phi\cos\mu - 2\cos\theta\sin\phi\sin\mu)^{1/2}} \right]$$

$$\sigma^2 = 0.003 + 0.00512v \qquad v = \text{wind speed (m/s) @ 12.4 m}$$

$$S*(\nu) = \frac{2}{1 + \text{erf}(\nu) + \dfrac{e^{-\nu^2}}{\nu\sqrt{\pi}}} \qquad \nu = \frac{\tan\phi}{\sigma}$$

Figure 1. Glint and imaging geometry for the first-order mean brightness model of Cox and Munk,[3] modified for self-shadowing of waves by Saunders.[4] A reflecting facet, assumed flat, has a surface normal n that is inclined by the angle β from local up. The ensemble of facets composing the sea surface has a normal distribution of slopes, $b = \tan \beta$, which are isotropic, i.e., the distribution of α is uniform over $[0, 2\pi)$. When the viewer zenith ϕ, viewer azimuth θ, and solar zenith μ are known, the angle of incidence for a ray from the Sun to the viewer can be calculated. The slope required for the reflection to occur is also a function of ϕ, θ, and μ. The variance of slope, σ, as a function of wind speed was determined empirically by Cox and Munk. A correction for self-shadowing, $S*$, was derived by Saunders. We have employed the simplest model, which assumes no wind direction dependence and uses only the leading term in the probability distribution of Cox and Munk.

n = facet normal
i = incident ray
r = reflected ray
z = local up
l = look vector

μ = solar zenith
ω = angle of incidence
β = facet slope
α = facet orientation
η = wind direction

ϕ = viewing zenith
θ = viewing azimuth
x', y', z' = focal plane coordinates
f = focal length

where ρ is reflectivity, p is the wave slope probability distribution function, S^* is the Saunders shadowing factor, and σ is the root-mean-squared slope. The angles in Eq. 8 are defined in Fig. 1.

We model image formation such that angles (in the object space) map to positions on the detector array. The seeker naturally measures radiance, i.e., the output of a detector is proportional to the average radiance within its instantaneous field of view. Since the scattering parameter in Eq. 7 depends on both the viewing angles and solar angles defined in Fig. 1, we can map the viewing angles to the facet coordinates.

We have used the NATO Anti-Air Weapons System (NAAWS) environmental model,[7] a weather-scenario-based model of environmental conditions, to generate probability laws for atmospheric propagation parameters. This database is restricted to the North Atlantic Ocean, but similar data exist for most of the world's oceans. The database was constructed by determining what combinations of meteorological air masses are likely to occur over a particular region and their relative frequency of occurrence. Associated with each combination is a representative scenario consisting of measured data including atmospheric soundings, surface conditions, cloud cover and taxonomy, and rain rates.

We have used the LOWTRAN7[2] model to compute path propagations, solar irradiance, etc. This model consists of several vertical profiles of atmospheric conditions, including profiles for modifications such as volcanic dust. It is a band model of attenuation and transmittance of molecular species and an aerosol scattering model. LOWTRAN7 has been superseded by MODTRAN2,[1] which has a higher spectral resolution. We are adopting MODTRAN2 in our current work.

COMPUTING TEMPORALLY AVERAGED SEA RADIANCE

We used the basic models to calculate the average brightness of the sea surface. LOWTRAN7, and its embedded Navy maritime model of the marine boundary layer as a function of wind speed, was used to calculate solar irradiance of the surface, sky radiance, path transmittance, path radiance, and apparent-effective boundary radiance as a function of wind speed for several slant paths in the 3.5- to 5.0-μm waveband. Values for intermediate ranges or angles were obtained using interpolators. Sky and solar irradiance were interpolated with piecewise cubic interpolators.[8] Path transmittance was interpolated using

$$\tau(x) = \exp\left(\sum_{i=0}^{3} a_i x^i\right), \qquad (9)$$

where the coefficients a_i are numerically determined with MODTRAN2 data. Path radiance and apparent-effective blackbody radiance were interpolated with the piecewise cubic polynomial of radiance as a function of the logarithm of range (Fig. 2).

Assuming that the incident solar radiation is unpolarized, the appropriate reflectivity of the sea surface is the average of the plane and perpendicularly (with respect to the plane of incidence) polarized reflection coefficients. We employed an effective index method[9] to compute seawater reflectivity as a function of incidence angle, using an index[10] of 1.33 evaluated at 4 μm, and an adsorption[11] of 200 cm^{-1}.

Applying these calculations to our approximation (Eq. 8), we calculated the radiance of the sea surface as a function of sensor zenith angles for low-altitude viewers and solar zenith angles around the specular point, and as a function of wind speed. Several interesting results emerge from this calculation. Typically, the brightest point on the sea surface occurs with the Sun above the specular direction because of path attenuation from the sea surface to the sensor. The apparent temperature of the sea surface can vary greatly, from a high of about 526 K for a calm sea to the sea temperature (about 288 K) for solar zeniths more than 10° from the specular point. The bright point also shifts closer to the sensor as the wind speed increases. Similar calculations, performed for comparison with other researchers' measurements,[5] were in substantial agreement, validating our model over a range of wind speeds and viewing geometries.

From a systems design standpoint, the temporally averaged glint model can be used to determine dynamic range requirements and "burn-through" thresholds. For example, Fig. 3 shows that given a 10-m/s wind speed, a target with an emissivity of one would need an apparent temperature rise of at least 62 K to exceed the mean radiance in the most intense portion of the glint corridor.

We also apply viewing transformations to create images of the scattered solar irradiance from the sensor's perspective (Fig. 4). These images are parameterized in terms of sea surface roughness, and they also show the effect of wind directions that are not collinear with the solar bearing.

COMPUTING THE TACTICAL LIKELIHOOD OF SEA GLINT

The model inputs for mean brightness are the viewer's zenith and solar-bearing relative azimuth, solar zenith, wind speed, and wind direction. We can make probabilistic assumptions regarding the geometry of an engagement and apply models of weather conditions in
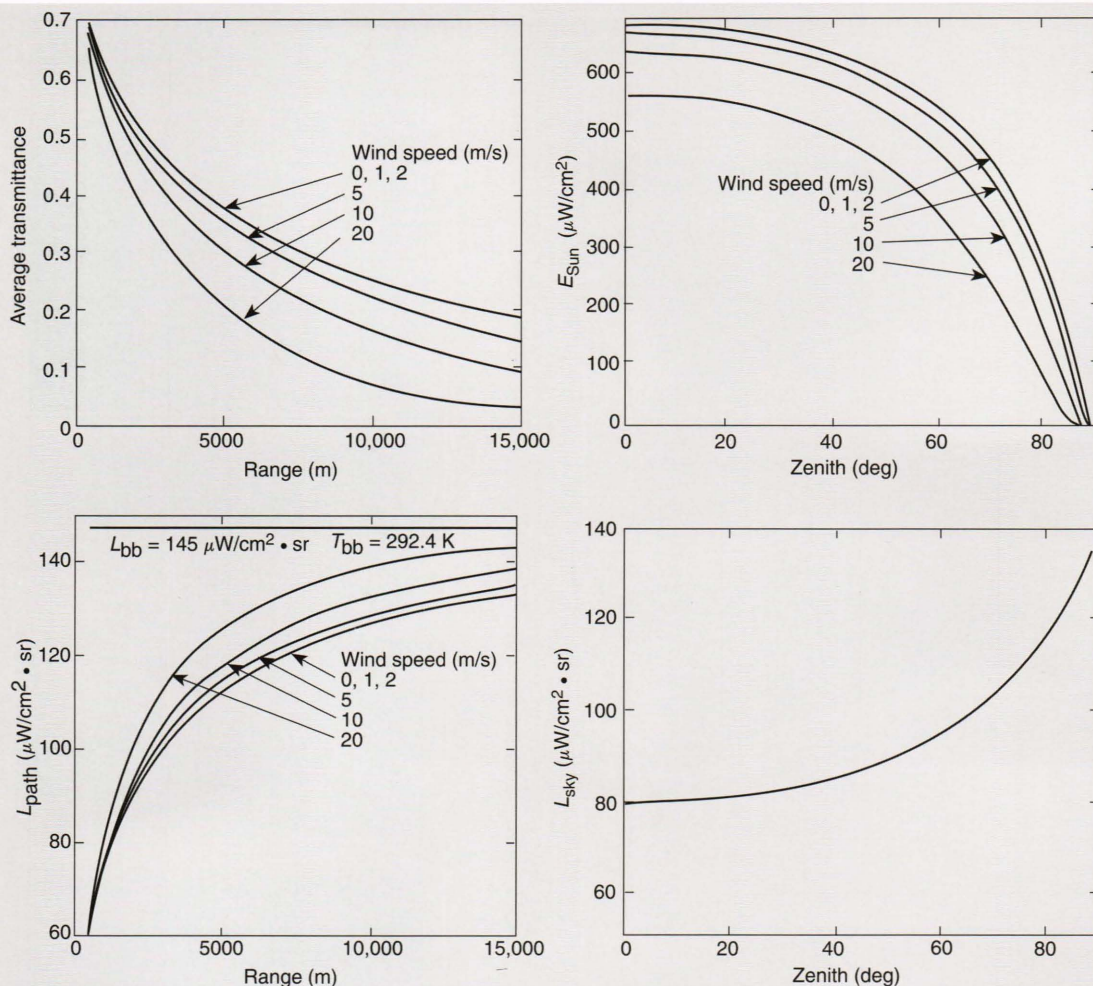
Figure 2. LOWTRAN7-calculated path and boundary properties as a function of wind speed in the 3- to 5-μm waveband and for slant paths from 130 to 2 m above the sea surface. As wind speed increases, more aerosols are lifted from the sea surface into the boundary layer and cause additional scattering (attenuation) in the ray path. Solar irradiance decreases as the Sun approaches the horizon because of the increased length of the optical path through the Earth's atmosphere. Path radiance approaches the blackbody limit as the optical path becomes very long, i.e., the atmosphere becomes optically thick. For an atmosphere at temperature $T_{bb} = 292.4$ K, the associated blackbody radiance of 145 μW/cm^2·sr is approached asymptotically. Sky radiance increases for the same reason.

the operational area to calculate, with Monte Carlo methods, the likelihood of encountering glint clutter.

The most suitable weather model had been developed as part of system effectiveness studies for the NAAWS. This database consists of representative weather scenarios and their probability of occurrence for various ocean regions. The taxonomy of weather scenarios was developed by studying air mass combinations, and the data include atmospheric soundings that we previously used to modify LOWTRAN7 atmospheric profiles. In this case, we only use wind speed and cloud cover data from the NAAWS database to develop nonparametric estimates of wind speed and cloud cover probability functions.

The detectability of a target is approximately determined by the contrast radiance of target with respect to background at the target location, i.e., not including path effects. This rough and optimistic approximation will be refined in future work. A more relevant method

uses our computational clutter model to generate realizations of clutter and then an actual detection algorithm to estimate contours of constant false alarm rate and detection probability in the scene. For now, we can use the mean contrast radiance approximation to construct, for a given target radiance, an indicator function that takes on a value of one when the scattered solar component exceeds our target threshold radiance. Thus the probability of glint, P_{glint}, is given by

$$P_{glint} = P_{illum} \int I(\Theta)p(\Theta)\,d\Theta, \qquad (10)$$

where I is the indicator function, Θ is the vector of engagement and weather parameters, $p(\Theta)$ is the density function of the parameters, and P_{illum} is the probability that the Sun illuminates the sea surface at the specific location. The results of a sample calculation are
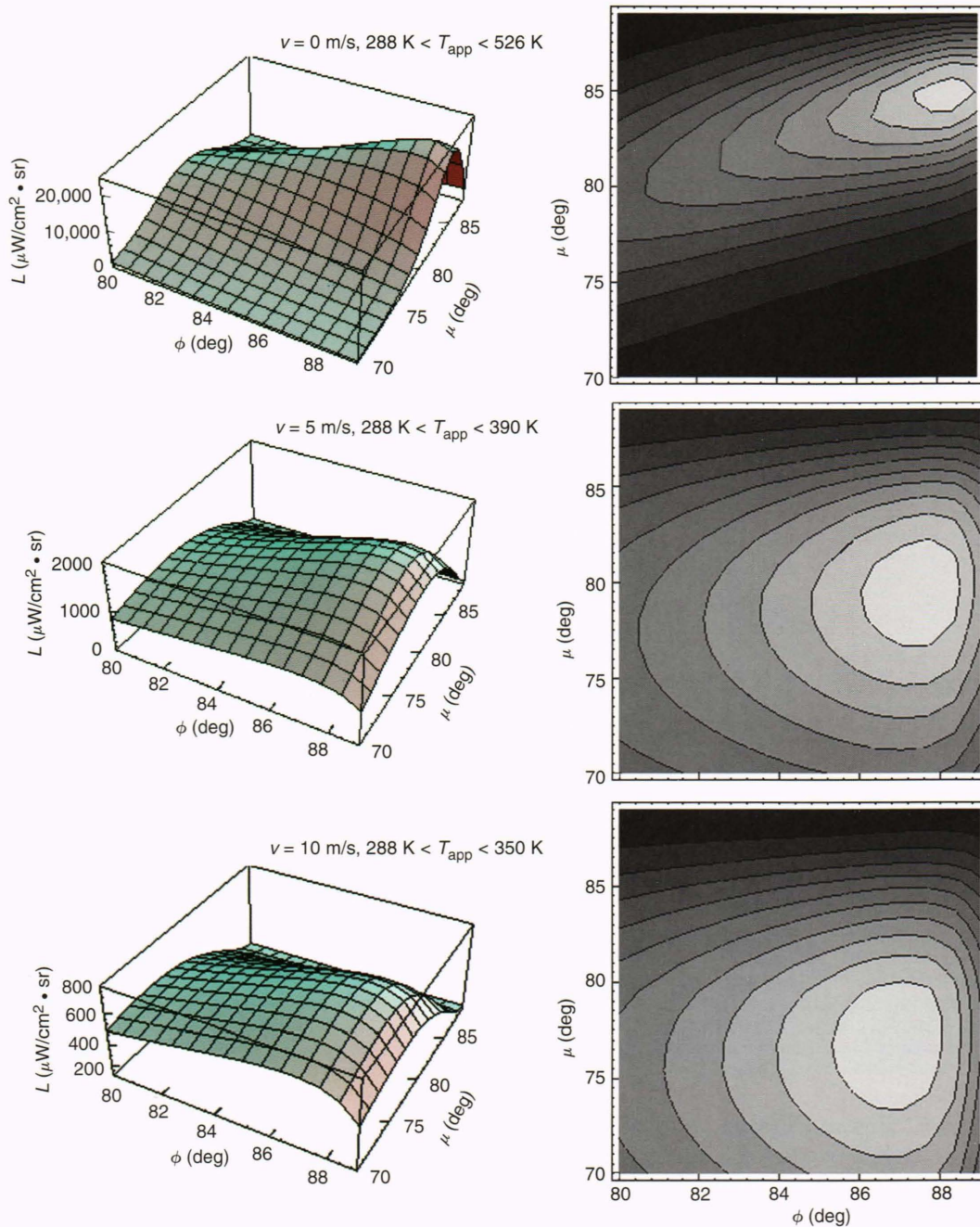
Figure 3. Midwave solar radiation scattered from the sea surface as a function of solar and sensor zenith angles. Results are shown for three wind speeds. The brightest point on the surface is shifted toward the observer (smaller ϕ) by progressively larger amounts as wind speed increases. This shift is due to the increasing attenuation of the path from the sea surface to the observer. T_{app} is the apparent temperature of the sea surface, assuming an emissivity of one, and v is wind speed.
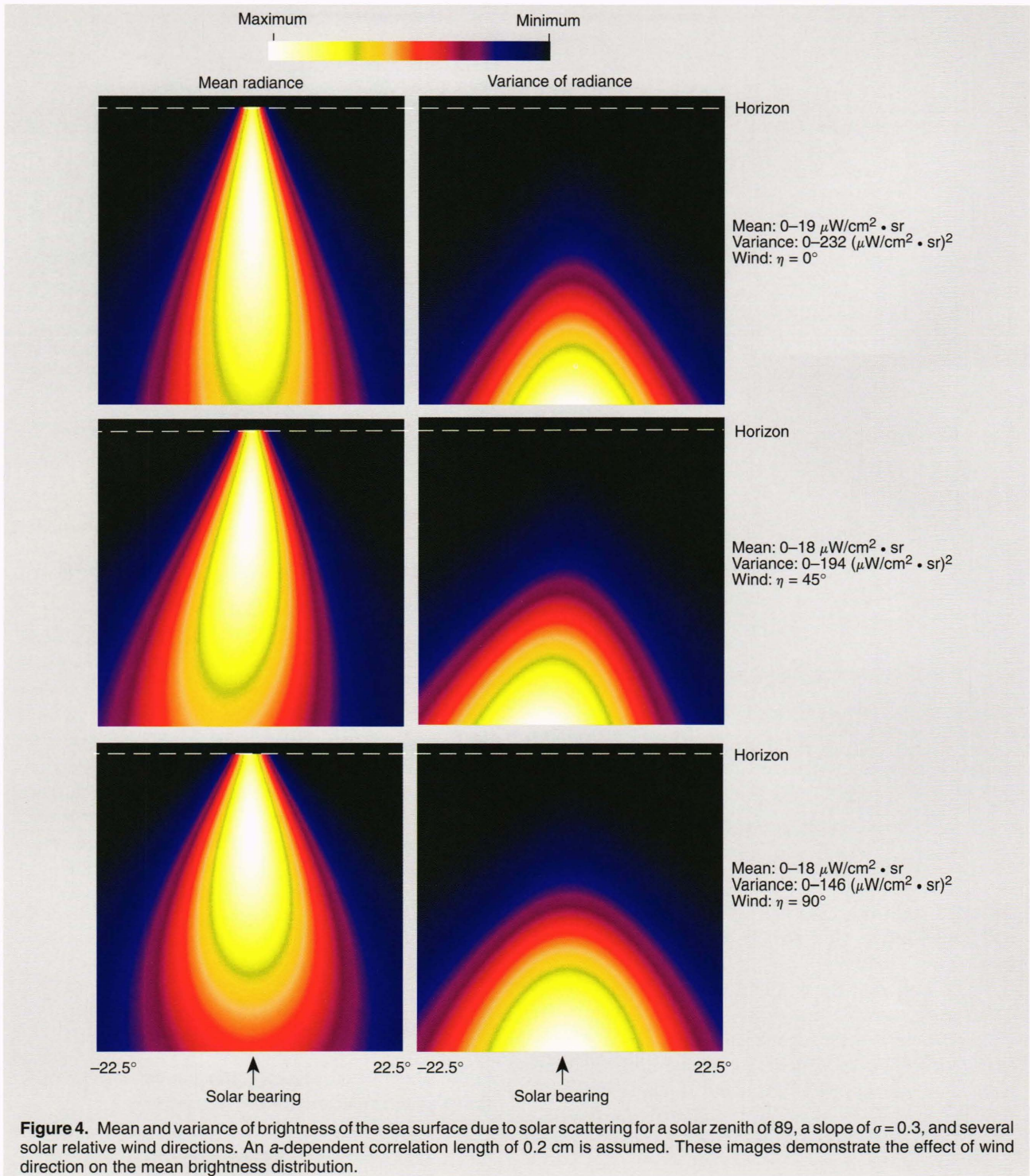
shown in Fig. 5, where time and location are uniformly distributed over 24 h and the North Atlantic Ocean, respectively.

COMPUTING FARS AND RADIANCE DISTRIBUTIONS

We conveniently and frequently assume that the distribution of clutter intensity is Gaussian. However, since intensity (the modulus squared of the incident electromagnetic wave) is always nonnegative, the distribution function of radiance is inherently non-Gaussian. In particular, detection systems that require very low FARs are sensitive to non-Gaussian tails of the filtered clutter image when the standard deviation of image radiance is on the order of the mean radiance. We used a time series of midwave glint images taken from Pt. Loma, California, with the General Dynamics

Figure 4. Mean and variance of brightness of the sea surface due to solar scattering for a solar zenith of 89, a slope of $\sigma = 0.3$, and several solar relative wind directions. An a-dependent correlation length of 0.2 cm is assumed. These images demonstrate the effect of wind direction on the mean brightness distribution.

Advanced Imaging Sensor to demonstrate the effect of non-Gaussian statistics on FAR and also calculate the temporal correlation of false detections.

We spatially filtered the time series of images with a Laplacian estimator (the filter computes an approximation to the Laplacian ∇^2 at each location in the image). Then each image was assigned a threshold at some multiplier of the standard deviation of the image, i.e., Gaussian constant FAR detection. Figure 6 describes the experiment graphically, and Fig. 7 shows the associated imagery.

Several outcomes are noteworthy. First, even with a segmentation into glinting and nonglinting regions, the FAR was 9 to 10 times the predicted (Gaussian) rate for the 3.0-σ threshold, and about 20 times the predicted rate for the 3.5-σ case (Table 1). If the threshold were increased further, this disparity would probably worsen. Evidently the clutter, even after filtering,

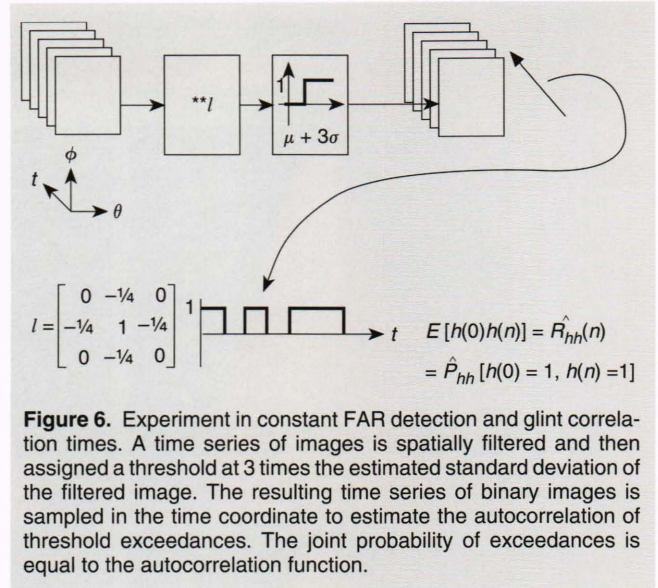(a)

(b)
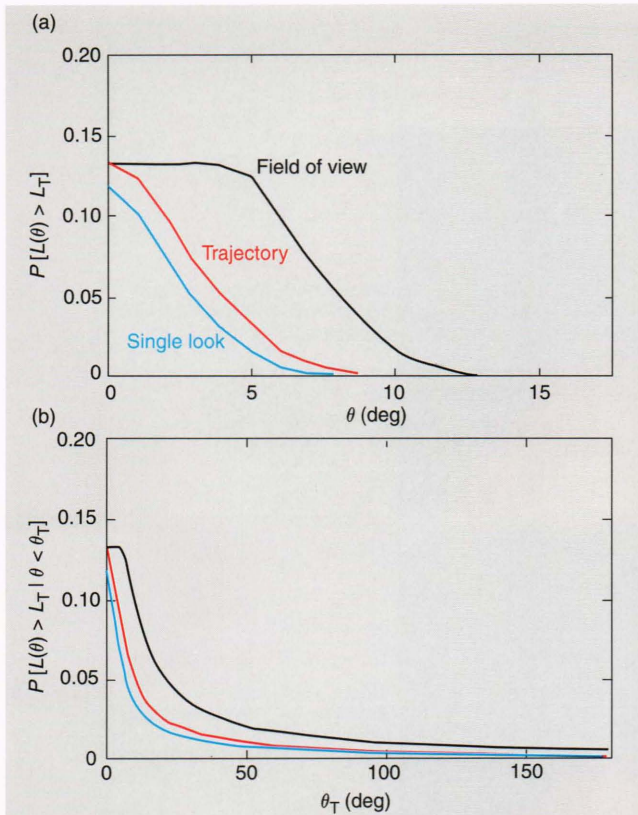
Figure 5. Probability that scattered midwave solar radiance exceeds a 0.25-W/cm^2·sr threshold L_T (a) at a single azimuth θ, and (b) for any azimuth less than θ_T. Single-look curves are for depression angles uniformly selected over 1.5 to 6° and time uniformly selected over 24 h, and they include the probability that the Sun is occluded by clouds. The trajectory curves are for probability of glint within the target trajectory from a 1.5 to 6° depression, and they include only the probability of a completely overcast sky. Field-of-view curves widen the trajectory to include a 4 × 4° field of view.

Figure 6. Experiment in constant FAR detection and glint correlation times. A time series of images is spatially filtered and then assigned a threshold at 3 times the estimated standard deviation of the filtered image. The resulting time series of binary images is sampled in the time coordinate to estimate the autocorrelation of threshold exceedances. The joint probability of exceedances is equal to the autocorrelation function.

does not meet the Gaussian assumption well enough and causes FARs that are an order of magnitude or larger than predicted.

Next, note that the correlation times of the thresholded images are on the order of 0.2 to 0.3 s. Other researchers have reported median glint times of 30 ms. Markov correlations with characteristic times of 70 ms have also been reported.[5] The issue of glint correlation time is significant in the design of false alarm rejection algorithms, which in turn affect imaging methods and search times.

Histograms of the glint images reveal the long-tailed nature of the intensities (Fig. 8), which apparently persists through the filtering process. Histograms of other data suggest that the distribution of intensities is gamma-like both inside and outside the glint region (Fig. 9). This result suggests, in the maximum entropy sense, that the expectation of the logarithm of intensity is constrained. We do not know the underlying physical basis for this phenomenon.

COMPUTING SPATIAL VARIANCE AS A FUNCTION OF RANGE

We assume that glint is a Bernoulli random process, i.e., that a location on the sea surface either images the Sun onto the observer or not, and that the surface is uniformly illuminated, as when there is no self-shadowing of waves. Then the mean and variance of the image of the sea surface radiance are not independent.

Let L_b and L_g be the background and glint radiance, respectively, and let P be the probability that the sea surface specularly reflects the Sun into the observer's line of sight. Then the mean and variance of the radiance at the observer are given respectively by

$$\langle L \rangle = L_b\left(1 - P\right) + L_g P,$$
$$\sigma^2_{L_0} = \left\langle L^2 - \langle L^2 \rangle \right\rangle = \left(L_b - L_g\right)^2\left(1 - P\right)P, \quad (11)$$
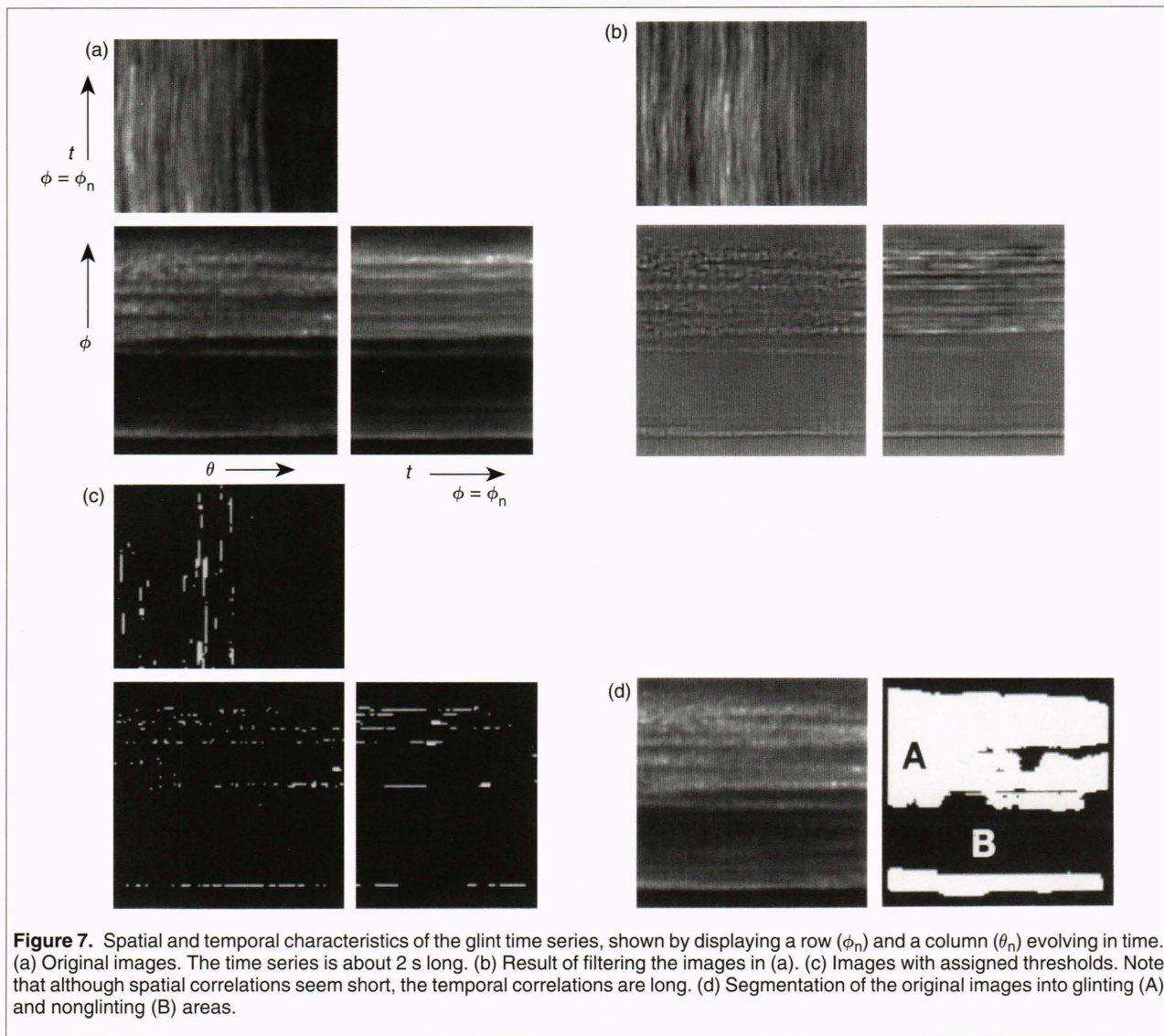
where $\langle \cdot \rangle$ denotes the expectation operator. The probability of specular reflection[3] is given by

$$P = \frac{\pi\epsilon^2 p}{4\cos(\omega)\cos^3(\beta)}, \quad (12)$$

where ϵ is the solar angular radius, p is the slope distribution function, ω is the angle of incidence, and β is the slope. The glint radiance L_g is given by

$$L_g = \frac{E_{Sun}\rho\cos(\omega)}{\pi\epsilon^2\cos(\beta)}, \quad (13)$$

Figure 7. Spatial and temporal characteristics of the glint time series, shown by displaying a row (ϕ_n) and a column (θ_n) evolving in time. (a) Original images. The time series is about 2 s long. (b) Result of filtering the images in (a). (c) Images with assigned thresholds. Note that although spatial correlations seem short, the temporal correlations are long. (d) Segmentation of the original images into glinting (A) and nonglinting (B) areas.

Table 1. Estimates of correlation time and FARs. Note that the Gaussian FAR is much smaller than the observed rates. In actual systems, this effect would be worse because the design FAR will be even farther out on the tails of the distribution ($\sigma > 5$).

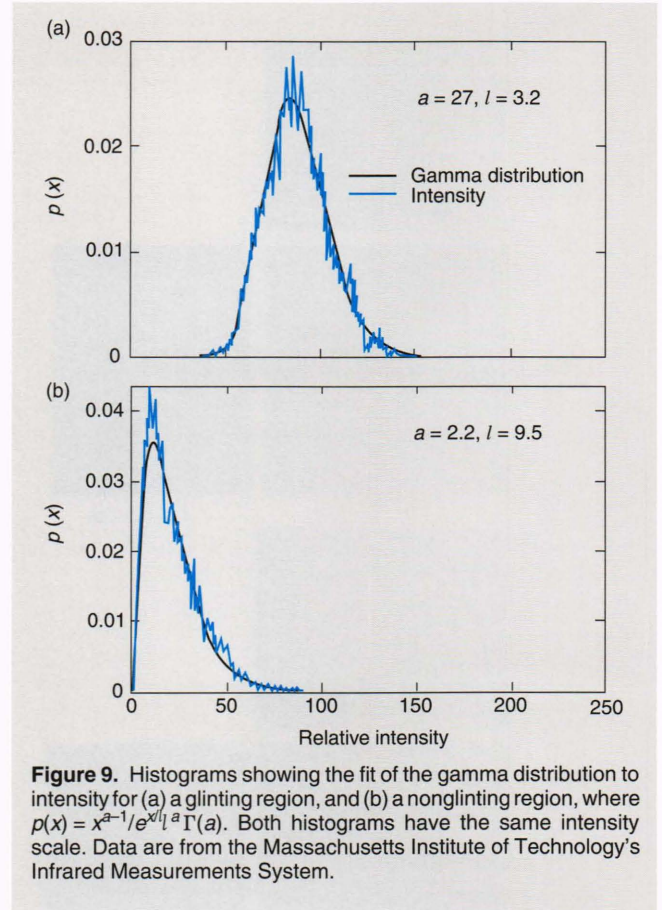|	Correlation time (s)		Observed FAR		
Threshold	Region A	Region B	Region A	Region B	Gaussian FAR
3.0σ	0.270	0.292	0.0096	0.014	0.0014
3.5σ	0.202	—[a]	0.0050	—[a]	0.00023

[a]Not measured.
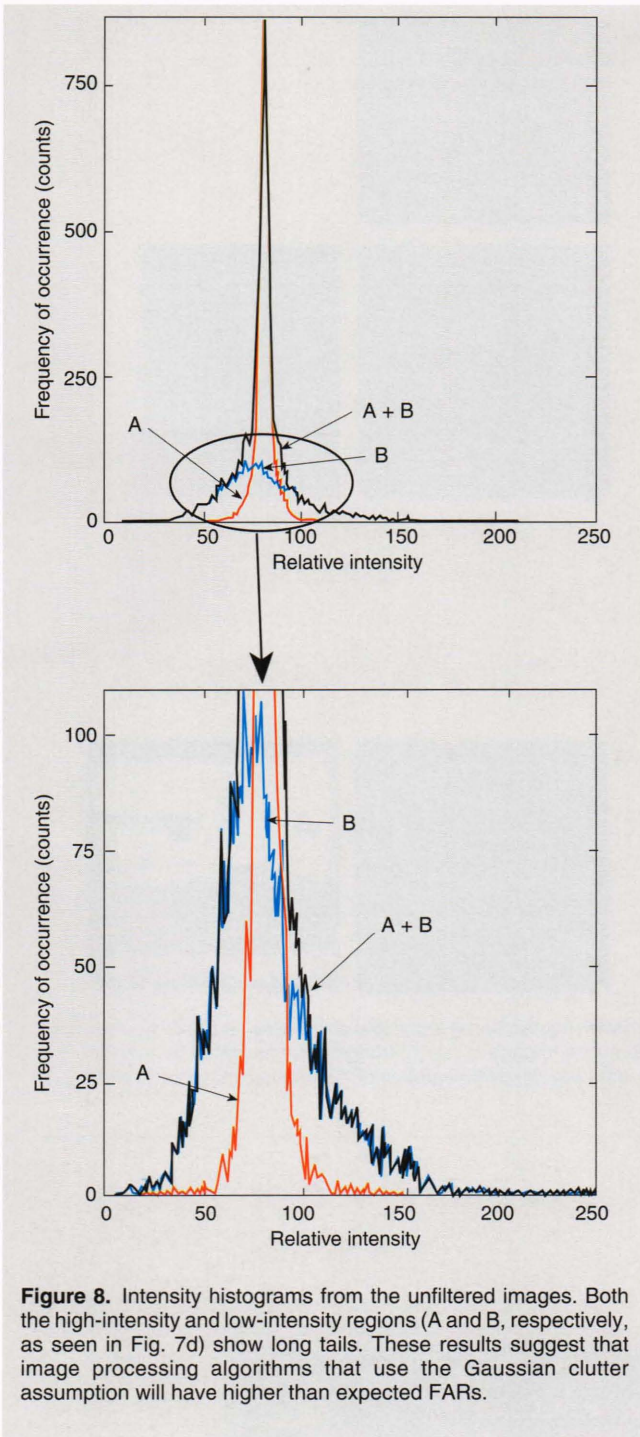
Figure 8. Intensity histograms from the unfiltered images. Both the high-intensity and low-intensity regions (A and B, respectively, as seen in Fig. 7d) show long tails. These results suggest that image processing algorithms that use the Gaussian clutter assumption will have higher than expected FARs.

Figure 9. Histograms showing the fit of the gamma distribution to intensity for (a) a glinting region, and (b) a nonglinting region, where $p(x) = x^{a-1}/e^{x/l} l^a \Gamma(a)$. Both histograms have the same intensity scale. Data are from the Massachusetts Institute of Technology's Infrared Measurements System.

where E_{Sun} is the solar irradiance. Substituting Eqs. 12 and 13 into Eq. 11, and (without loss of generality) assuming that $L_b = 0$, we arrive at the Cox and Munk expression for temporally averaged radiance:

$$\langle L \rangle = \frac{E_{Sun} \rho p}{4\cos^4 \beta} . \tag{14}$$

The glint variance is given by

$$\langle L^2 \rangle = \langle L \rangle^2 \left[\frac{1 - 4\cos^3 \beta \cos \omega}{\pi \epsilon^2 p} \right] . \tag{15}$$

Measurements by Fraedrich[5] indicate that, for low wind speeds, limited fetch (the distance over which waves can build up, or the distance in the upwind direction nearest land), and low observation angles, the temporal correlation of glint clutter is Markovian, with a characteristic time of about 70 ms. Thus the power spectral density of glint is given by

$$|\mathscr{F}\{L\}|^2 = \frac{C_0 f_0}{f_0^2 + f^2}$$
$$\langle L(t)L(t + \tau) \rangle = R_{LL}(\tau) \propto e^{-|\tau|/T} , \tag{16}$$

where $\mathscr{F}\{\cdot\}$ denotes the Fourier transform, f_0 is the characteristic frequency, T is the characteristic time (70 ms), C_0 is an arbitrary constant, and R_{LL} is the correlation function. However, we are interested in the correlation length of glint. We make the assumption

that the capillary wave dispersion relationship can be used to change correlation time to correlation length:

$$\omega^2 = \frac{vk^3}{\rho},\qquad(17)$$

where the viscosity v is 76.3 dyn/cm, k is the wavenumber in cm^{-1}, and the density ρ is 1.025 g/cm^3. The correlation length of the process, l, is then 0.210 cm. For $T = 0.3$ s, the corresponding value of l would be 0.554 cm.

The a-dependent[12] correlation area of the spatial random process, l^2, is between 0.044 and 0.307 cm^2. Suppose that the footprint of one seeker detector on the sea surface is A. The corresponding solid angle is the detector instantaneous field of view (Ω_d). If the footprint is large, i.e., $\sqrt{A} \gg 0.044$, the image random process has a mean given by Eq. 14 and a variance given by

$$\sigma_L^2 = \frac{\sigma_{L_0}^2 \, l^2 \cos\phi}{\Omega_d r^2},\qquad(18)$$

where r is the range to the sea surface. Note that the effective averaging area A is given by

$$A = \frac{\Omega_d r^2}{\cos\phi}.\qquad(19)$$

The footprint of the detector solid angle for low grazing angle images is stretched by $\cos\phi$ in one direction, and the averaging area is much larger than in the nadir case. This is one of the reasons that clutter washes out toward the horizon. Even if the correlation length is not determined by Eq. 17, as long as $A \gg l^2$, the result maintains its functional form to within a multiplicative constant.

The images shown in Fig. 4 correspond to glint patterns that are temporally and spatially averaged (over a 1.0-mrad Ω_d) from several perspectives. They were calculated using Eq. 18.

EMPIRICAL TEXTURE MODELS

Given an image or a times series of images of the sea surface, one can attempt to parametrically model the higher-order statistics of the scene. It has been shown that the maximum entropy joint distribution function for a process on a lattice can be specified as a conditional probability distribution over a set of interaction neighborhoods called cliques.[13] These models are generally referred to as Markov random fields, and they have seen application in various texture modeling and pattern recognition tasks.

We attempted to apply an autobinomial[14] texture model to the texture of a nadir-viewed glinting sea. Parameters were estimated using a maximum likelihood method,[13] and sample textures were then generated using both a Gibbs relaxation method[15] and a Metropolis method[14] (Fig. 10). We experienced problems with

(a)

(b)
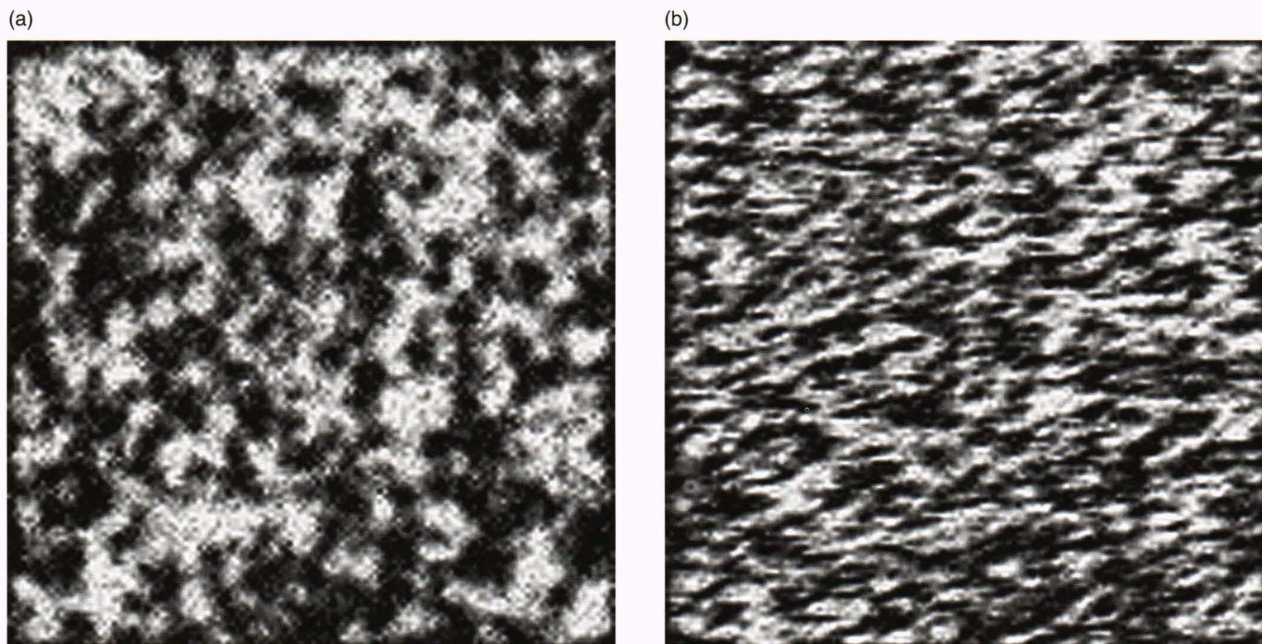
Figure 10. Autobinomial Markov random field textures. Image (a) illustrates the use of isotropic clique parameters, and image (b) emphasizes correlations in the horizontal direction.

parameter estimate convergence: the resultant textures did not appear to be a good fit, although no quantitative comparisons were made. We also found that the Gibbs method tended to form either totally disordered images, i.e., white noise, or to "crystallize" into totally organized images, i.e., constants. Use of an exchange algorithm (in the Metropolis method) allowed us to constrain the asymptotic distribution of the field and avoid problems.

We hope to continue pursuing these methods using Gauss–Markov random fields,[16,17] which suffer from the Gaussian univariate distribution. For large mean values of the clutter, however, this drawback may not be a problem, or perhaps modifications for long-tailed behavior can be added. Of particular interest to us will be the ability to model clutter in two spatial coordinates and the temporal coordinate. If that is possible, realizations of the random process computed with periodic boundary conditions would provide an "infinite loop" scene for dynamic hardware-in-the-loop testing.

RAY TRACING MODELS

Gravity wave structure is visible in certain viewing geometries (see the boxed insert on glint phenomena). The clutter is a mixed-scale phenomenon, with long-scale variations caused by gravity wave shadowing of the solar illumination and small-scale variations caused by the capillary wave roughness of the sea surface. To the first order, the clutter is then a multiplicative process, with illumination multiplied against surface albedo. Since the Cox and Munk scattering parameter is really a bidirectional reflectance distribution function (BRDF), we can write the process as

$$L(\phi, \theta, \mu, \eta) = \xi(\phi, \theta, \mu, \eta) E(\phi, \theta, \mu), \qquad (20)$$

where $E(\phi, \theta, \mu)$ is the irradiance of the facet being viewed, and the additional parameter η is wind direction in the solar bearing relative coordinates.

We have computed this radiance function with our Seascape clutter model. Seascape is a ray tracing program[18] whose discrete waveheight field synthesis is consistent with existing waveheight models,[19] and in which the Cox and Munk BRDF is associated with each wave facet (Fig. 11). We have also applied the dynamics of wave motion to the realization in order to animate the clutter process.

Our ray tracing model currently includes path attenuations, uniform skylighting, and graybody emissions of the sea and atmosphere that were computed using the approximations in Eq. 7. Viewpoints can be animated along with the sea surface, and graybody targets can be modeled with constructive solid geometry. We have several animation sequences for use in an infrared seeker signal processing design. Figure 12 shows an example of synthetic clutter.

Seascape is computationally intensive. The example sequence in Fig. 12, which was 100 frames long, required about 8 teraflop (8×10^{12} floating point calculations) and was computed in 200 h on a Silicon Graphics Indigo workstation with an R3000 processor. We have been able to distribute the calculation over many computers on the APL network. This parallel distributed version of Seascape has been benchmarked at 10 times faster than the single-workstation calculation. We anticipate that speedups of 100-fold or more will be achievable in this way.

The straightforward implementation of sea-height fields in a ray tracer is memory intensive. The image in Fig. 12 represents a patch of the ocean that is 14 km long and whose average width is 3.5 km, with a lattice spacing of 1 m. A direct implementation would then require about 0.4 gigabyte for synthesis and 0.7 gigabyte for ray tracer representation. We exploit certain symmetries and object-oriented constructs to reduce the memory required by a factor of 40.

Seascape is not currently validated, but it does demonstrate known phenomena. The mean glint patterns reproduce the Cox and Munk spatial patterns (Fig. 4). The radiance distribution functions of synthesized clutter reproduce the gamma-like distributions of measured clutter (Fig. 8). Simulation of small length scales reproduces short-time-scale scintillations, whereas simulations of large length scales reproduce gravity wave shadowing correlations with long time scales. The combination of path attenuation and spatial averaging by
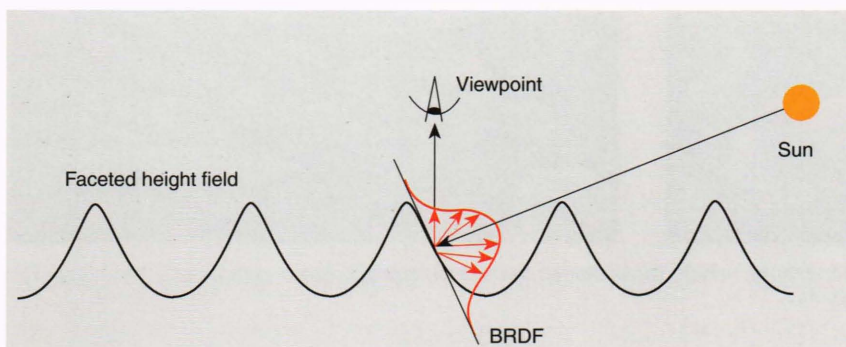
Figure 11. Two-scale ray tracing model of glint clutter. Conventional ray tracing methods determine the illumination of the surface at the (relatively large) scale of the faceted surface representation, whereas small-scale roughness is stochastically modeled by the bidirectional reflectance distribution function.
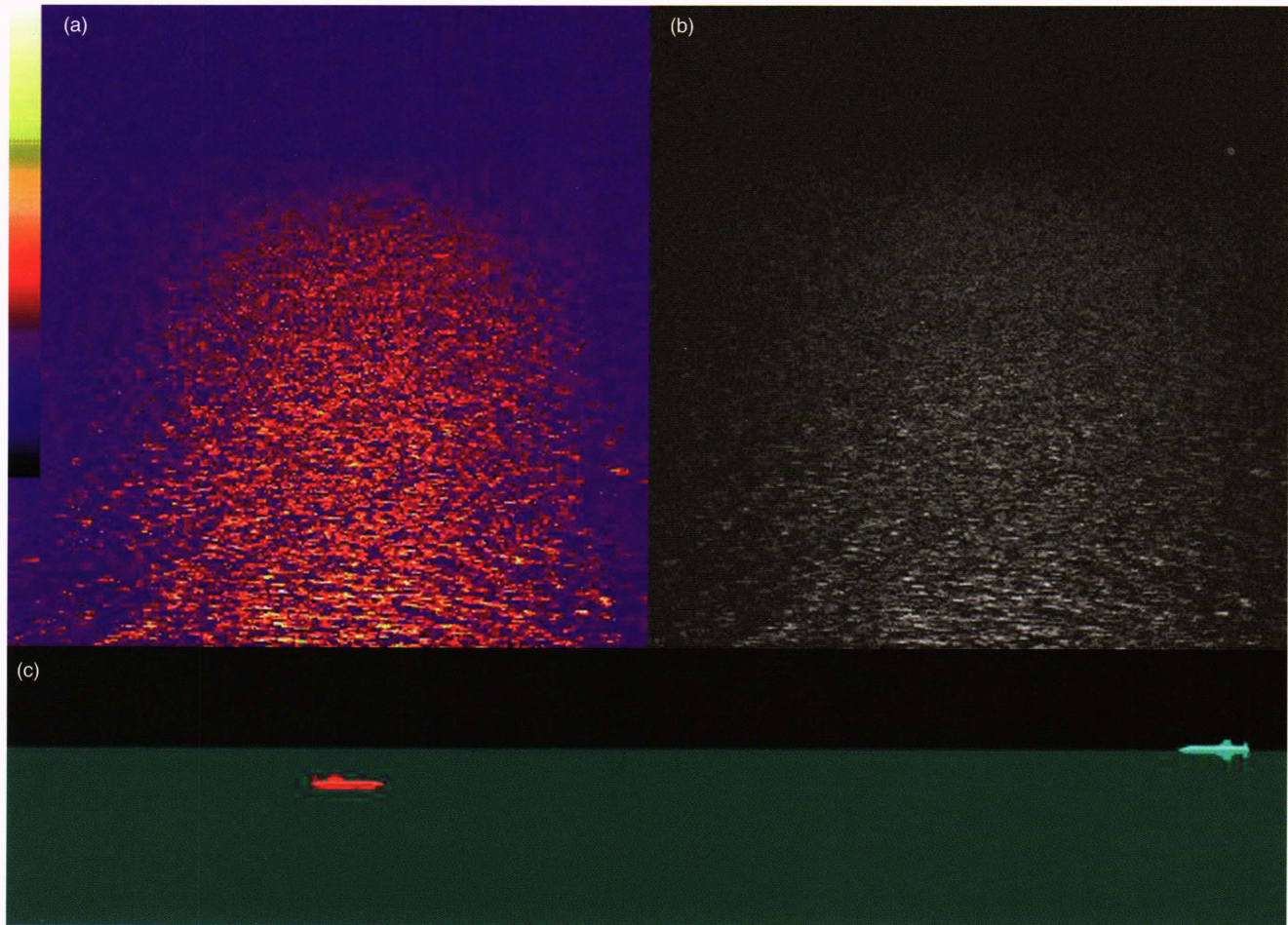
Figure 12. Single frame of an animation. The animation shows the view from a defending missile's seeker as it engages a sea-skimming attacking missile in solar sea glint. Part (a) is a pseudocolored rendition of the radiance image, which is seen in (b). Part (c) is a side view of the engagement, where the attacking missile is red and the defending missile is green. An MPEG (Motion Picture Experts Group) of this animation and of measured data is located at the URL (Uniform Resource Locator) http://fsdwww.jhuapl.edu/.

the imager reproduces the washed-out appearance of the horizon in the midwave.

We are radiometrically validating Seascape in the 2.3- to 4.6-m waveband. We have made measurements of sea glint using a calibrated indium antimonide focal plane array camera and are in the process of comparing our field measurements with ray tracer outputs (see the article by Constantikes and Claussen in this issue). Preliminary checks have shown that measurements are in rough agreement with predictions.

SUMMARY

We have applied existing models of mean sea brightness, propagation, and weather to the evaluation of seeker design and the tactical importance of sea glint. We used the models to compute example scattered mean and variance of radiance patterns from low altitude for various values of sea roughness and wind direction.

These patterns can be used to approximate where target detection may take place. They can also be used in a simple signal processing model. Experimental evidence shows that the non-Gaussian nature of sea radiance is significant in the design of detection systems, and, in particular, that the gamma-like distribution function persists through linear filtering and can cause inordinately high FARs. Other approaches to generating sea image statistics include Markov random field methods and ray tracing methods. The ray tracing methods hold great promise for the synthesis of realistic sea clutter images, including temporal and spatial behaviors and both target and seeker motions. We are in the process of validating our ray tracing model using measured data.

REFERENCES

[1] Berk, A., Bernstein, L. S., and Robertson, D. C., *MODTRAN: A Moderate Resolution Model for LOWTRAN7*, GL-TR-89-0122, Air Force Geophysics Laboratory, Hanscom AFB, MA (1989).

[2] Kneizys, F. X., Shettle, E. P., Abreu, L. W., Chetwynd, J. H., and Anderson, G. P., *Users Guide to LOWTRAN7*, AFGL-TR-88-0177, Air Force Geophysics Laboratory, Hanscom AFB, MA (1988).

[3] Cox, C., and Munk, W., "Measurement of the Roughness of the Sea Surface from Photographs of the Sun's Glitter," *J. Opt. Soc. Am.* **44**(11), 838–850 (1954).

[4] Saunders, P. M., "Radiance of the Sea and Sky in the Infrared Window 1000–1200 cm^{-1}," *J. Opt. Soc. Am.* **58**(5), 645–652 (1968).

[5] Fraedrich, D. S., "Spatial and Temporal Infrared Radiance Distributions of Solar Sea Glint," *SPIE Ocean Optics IX* **925**, 392–397 (1988).

[6] Boyd, R. W., *Radiometry and the Detection of Optical Radiation*, Wiley, New York (1983).

[7] Bégin, R., Cross, R. K., Picard, G., Pindam, M., and Savoie, F., *NAAWS System Performance Analysis Handbook: The NAAWS Environmental Database*, Defence Research Establishment, Valcartier, Canada (1989).

[8] Wolfram, S., *Mathematica*, 2nd Ed., Addison-Wesley, New York (1991).

[9] *The HandBook of Optics*, W. G. Driscoll (ed.), McGraw-Hill, New York, p. 10-10 (1978).

[10] *The Infrared Handbook*, Office of Naval Research, Washington, DC, Fig. 3-109, p. 3-105 (1985).

[11] *The Infrared Handbook*, Office of Naval Research, Washington, DC, p. 3-71 (1985)

[12] Papoulis, A., *Probability, Random Variables, and Stochastic Processes*, McGraw-Hill, New York, 2nd Ed., p. 217 (1984).

[13] Besag, J., "Spatial Interaction and the Statistical Analysis of Lattice Systems," *J. Proc. Royal Stat. Soc. Ser. B* **36**, 192–236 (1974).

[14] Cross, G. R., and Jain, A. K., "Markov Random Field Texture Models," *IEEE Trans. Pattern Analysis and Machine Intelligence* **PAMI-5**(1), 25–39 (1983).

[15] Geman, S., and Geman, D., "Stochastic Relaxation, Gibbs Distributions, and the Bayesian Restoration of Images," *IEEE Trans. Pattern Analysis and Machine Intelligence* **PAMI-6**(6), 721–741 (1984).

[16] Dubes, R. C., and Jain, A. K., "Random Field Models in Image Analysis," *J. Applied Statistics* **16**(2), 131–164 (1989).

[17] Cressie, N. A. C., *Statistics for Spatial Data*, Wiley-Interscience, New York (1993).

[18] Glassner, A. S. (ed.), *An Introduction to Ray Tracing*, Academic Press, London (1989).

[19] Bjerkas, A. W., and Riedel, F. W., *Proposed Model for the Elevation Spectrum of a Wind-Roughened Sea Surface*, STD-R-041, The Johns Hopkins University Applied Physics Laboratory, Laurel, MD (1979).

THE AUTHOR
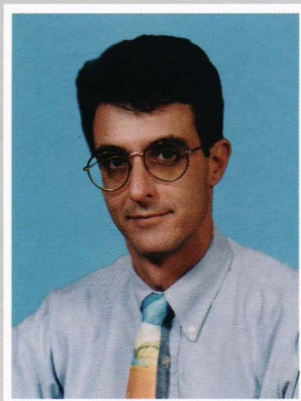
KIM T. CONSTANTIKES is a Senior Staff engineer in APL's Fleet Systems Department. He received his B.S. degree in applied physics in 1983 from Ohio University. He then attended Carnegie Mellon University with a Benjamin Franklin Fellowship and received an M.S. degree in electrical and computer engineering in 1985. At Carnegie Mellon, he researched topics in pattern recognition and sensors in the Smart Sensors Laboratory of the Robotics Institute. Mr. Constantikes joined APL's Electro-Optical Systems Group in 1985, where he has worked on various computational and algorithmic aspects of imaging systems used for target acquisition, tracking, and recognition, as well as image-matching navigation. His current interests include image and scene modeling, image processing algorithms, target detection in clutter, and computer graphics. His e-mail address is Kim.Constantikes@jhuapl.edu.